### Realization of Trapped Ion Dynamics in the Strong-Field Regime and Non-Markovianity

Kamran Rehan, <sup>1, 2, 3, \*</sup> Hengchao Tu, <sup>2</sup> Menglin Zou, <sup>2</sup> Zihan Yin, <sup>2</sup> Jing-Ning Zhang, <sup>1</sup> and Kihwan Kim<sup>1, 2, 4, 5, †</sup>

<sup>1</sup>Beijing Academy of Quantum Information Sciences, Beijing 100193, China

<sup>2</sup> State Key Laboratory of Low Dimensional Quantum Physics,

Department of Physics, Tsinghua University, Beijing 100084, China

<sup>3</sup> Department of Physics, The University of Haripur, KP, Pakistan

<sup>4</sup> Hefei National Laboratory, Hefei 230088, China

<sup>5</sup> Frontier Science Center for Quantum Information, Beijing 100084, China

Probing quantum dynamics in the strong-field regime is critical for advancing our understanding of controlled quantum systems and developing robust quantum technologies. In this work, we experimentally investigate the dynamics of a trapped-ion where the Rabi frequency  $\Omega$  approaches the vibrational mode frequency  $\nu$ , pushing the system beyond the weak-field regime, where non-trivial quantum correlations emerge. We begin by setting the detuning  $\delta$ —the frequency offset between the qubit transition and the driving field—to zero and varying  $\Omega$  from low to high values, eventually reaching vibration frequency. Using quantum state tomography, we reconstruct the density matrix and track its evolution to assess non-Markovianity (NM), revealing significant memory effects governed by the interplay between internal and motional degrees of freedom. Furthermore, by exploring the dynamics across various parameter pairs  $(\Omega, \delta)$ , we find that NM does not always increase monotonically with  $\Omega$  for a fixed  $\delta$ . Strikingly, when the condition  $\delta^2 + \Omega^2 = \nu^2$ , is met, the NM exhibits a circular pattern of maxima. At this parameter combination, the system's Hamiltonian takes a form similar to the Jaynes-Cummings model, enabling the possibility of analytical insights into the observed dynamics. These results go beyond the conventional carrier and sideband regimes. uncovering novel features of strong-field quantum dynamics. Our findings establish a pathway for using trapped-ion platforms to investigate non-Markovianity, coherent control, and the fundamental behavior of open quantum systems in extreme regimes.

Controlling quantum states in atomic systems via laser-induced coherent interactions is central to both quantum optics and quantum information science. In one of the most prominent quantum technologies to date—laser-cooled trapped ions [1, 2]—laser illumination induces coupling between internal (electronic) and external (vibrational) degrees of freedom. The former can typically be modeled as a two-level system (qubit), and the latter as a simple harmonic oscillator [1–5]. In the weak-field regime, where the laser Rabi frequency  $\Omega$  is much smaller than the vibrational frequency  $\nu$ , the dynamics is well described by effective models such as the carrier and sideband Hamiltonians, derived via the standard rotating wave approximation (RWA) [1, 2]. However, when  $\Omega \sim \nu$ , due to stronger laser driving, the RWA breaks down, and alternative descriptions must be employed [6]. This regime is particularly appealing, as it allows for faster dynamical evolutions compared to the well-established case  $\Omega \ll \nu$ . Since real quantum systems have finite coherence times, enabling faster state manipulations is highly desirable.

The first theoretical proposals involving strong lasers  $(\Omega \sim \nu)$  emerged in the context of quantum computing, aiming to implement fast quantum gates [7, 8]. More recently, this regime has been explored for reconstructing the motional Wigner function [9], with advantages over weak-coupling approaches. It has also been proposed as a platform for quantum thermal devices, where effects such as negative differential heat conductivity and heat

rectification have been observed [10], providing insights into the thermal behavior of strongly driven trapped ions.

Meanwhile, over the past decade, significant progress has been made in identifying and quantifying memory effects—also known as non-Markovian (NM) behavior in open quantum systems. Modern approaches characterize such effects via the breakdown of dynamical map divisibility [11], information backflow [12], and other criteria [13–20]. In the era of noisy intermediate-scale quantum (NISQ) devices [21], studying open quantum systems has become increasingly relevant for mitigating decoherence. Memory effects from coupling to structured baths are especially relevant in technologies ranging from optical systems [22–26] and NMR [27] to superconducting qubits [28–30] and trapped ions [5, 31, 32], the latter typically operating in the weak-laser regime  $\Omega \ll \nu$ .

In our setup, where the dynamics can be accelerated by increasing the laser power such that  $\Omega \sim \nu$ , it is especially relevant to investigate how NM emerges in the qubit due to its coupling with the motional degrees of freedom [33, 34]. Here, we report what appears to be the first experimental study of trapped ions in this strong-laser regime. We focus on the non-Markovian dynamics of the internal degrees of freedom, i.e., the qubit, which forms an open quantum system coupled to a structured bath consisting of the external vibrational motion and Markovian dephasing noise. The latter is modeled via an effective dephasing rate  $\gamma$ , determined experimentally. Memory effects in the qubit arise from laser-induced cou-

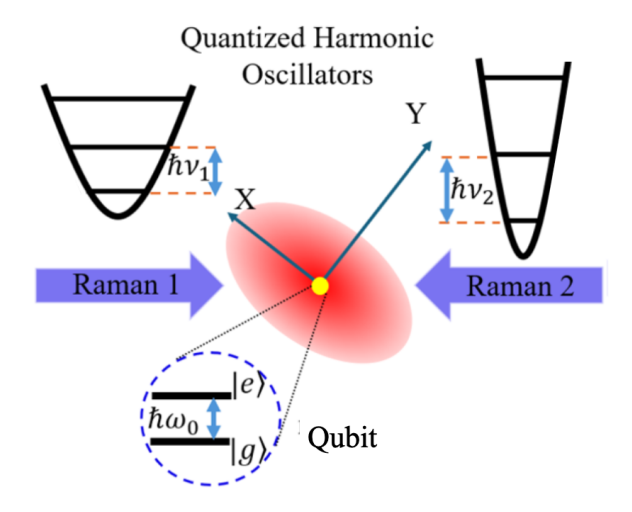


FIG. 1. Schematic diagram of our system. The elliptical trapping potential of the Paul trap gives rise to two radial motional modes with frequencies  $\nu_1$  and  $\nu_2$ , corresponding to vibrations along the x and y directions, respectively. Two electronic (internal) states form a qubit, which is coupled to each vibrational mode via two sets of Raman lasers.

pling to motion [35]. When the lasers are turned off, the qubit follows purely Markovian dephasing at rate  $\gamma$ .

Letting  $\rho(t)$  denote the density operator of the full system (internal + external), we study the dynamics of the reduced qubit state  $\rho_{\text{qubit}} := \text{tr}_{\text{mot}}[\rho]$ , obtained by tracing out the motional part. In the absence of coupling,  $\rho_{\text{qubit}}$  undergoes simple exponential dephasing at rate  $\gamma$ . However, under strong coupling to motion, the dynamics becomes richer, with memory effects emerging due to the structured environment. Our goal is to experimentally probe this NM behavior under controlled variations of the Rabi frequency  $\Omega$  and the detuning  $\delta = \omega_0 - \omega_L$ , where  $\hbar\omega_0$  is the energy difference between the qubit levels  $|e\rangle$  and  $|g\rangle$ .

The system is shown in Fig.1. The qubit consists of the hyperfine states  $|g\rangle \equiv |F=0,m_F=0\rangle$  and  $|e\rangle \equiv |F=1,m_F=0\rangle$  of a single trapped <sup>171</sup>Yb<sup>+</sup> ion, within the  $^2S_{1/2}$  ground-state manifold, separated by a hyperfine splitting of  $\omega_{\rm hf}=2\pi\cdot 12.642812$  GHz [36–42]. The structured environment includes two radial motional modes with frequencies  $\nu_1(\nu_2)/(2\pi)=2.32$  (3.16) MHz, due to the anisotropic Paul trap. These correspond to vibrations along x and y, with Lamb-Dicke parameters  $\eta_1(\eta_2)=0.069$  (0.072). The higher frequency along y reflects tighter confinement, as illustrated by the red ellipse in Fig.1 [38].

In the rotating frame defined by the laser frequency  $\omega_L$ , our trapped-ion system is described by the Hamiltonian

$$H = \frac{\hbar \delta}{2} \sigma_z + \hbar \nu_1 a_1^{\dagger} a_1 + \hbar \nu_2 a_2^{\dagger} a_2 + \frac{\hbar \Omega}{2} [\sigma_+ e^{i\eta_1(a_1 + a_1^{\dagger})} + \sigma_+ e^{i\eta_2(a_2 + a_2^{\dagger})} + \text{h.c.}], (1)$$

where  $\sigma^{\pm} \equiv (\sigma_x \pm i \sigma_y)/2$  are the spin-flip operators,  $\sigma_{x,y,z}$  are the usual Pauli matrices,  $\hbar$  is the reduced Planck constant,  $a_1$  and  $a_2$  are the annihilation operators for two orthogonal motional modes with angular frequencies  $\nu_1$  and  $\nu_2$ , respectively, and the last term represents the laser-induced spin-vibration interaction, with  $\Omega$  denoting the Rabi frequency.

Our experiments also reveal that the system undergoes qubit dephasing, such that the evolution of the total system is governed by

$$\frac{d\rho}{dt} = -i[H, \rho] + \gamma(\sigma_z \rho \sigma_z - \rho), \tag{2}$$

where H is given by Eq. (1), and  $\gamma$  is the dephasing rate. A key signature of non-Markovianity (NM) in qubit systems is the nonmonotonic time evolution of the trace distance between two initially antipodal states,  $\rho_1(0)$  and  $\rho_2(0)$ , defined as

$$D(\rho_1(t), \rho_2(t)) := \frac{1}{2} \operatorname{tr} |\rho_1(t) - \rho_2(t)|, \tag{3}$$

where  $|A| := \sqrt{A^{\dagger}A}$  and  $\rho_1(t)$  ( $\rho_2(t)$ ) is the state  $\rho_1(0)$  ( $\rho_2(0)$ ) evolved according to Eq.(2). For a pure Markovian processes, the trace distance decreases monotonically over time, indicating an irreversible loss of information. In contrast, any temporary increase in the trace distance signals non-Markovianity in the dynamics governed by Eq.(2) [31, 43].

To quantify NM, one analyzes the time derivative of the trace distance:

$$\sigma(t) := \frac{d}{dt} D(\rho_1(t), \rho_2(t)), \tag{4}$$

and evaluates the functional

$$NM := \max_{\rho_1, \rho_2} \int_{\sigma > 0} dt \sigma(t), \tag{5}$$

where the maximization is taken over all pairs of antipodal initial states  $\rho_1(0)$  and  $\rho_2(0)$ , and the integral is performed over time intervals where  $\sigma > 0$ . This optimization step is what grants Eq. (5) the status of a proper measure [31, 43]. In our analysis, however, we are interested only in the qualitative behavior of NM and therefore omit the maximization step.

Here, we report the experimental observation of trapped-ion dynamics in the strong-laser regime, and we find and characterize the non-Markovian behavior of the internal (electronic) degree of freedom, or qubit, whose states  $\{|g\rangle,|e\rangle\}$  are described in Fig. 1. This work establishes a novel framework for trapped-ion control, extending the manipulation of the system beyond the established carrier and sideband interactions valid only for weaker lasers.

To this end, we study the evolution of initial product states  $\rho(0) = \rho_S(0) \otimes \rho_E(0)$ , where the system is initialized in one of two antipodal states:  $\rho_S^1(0) \equiv |+\rangle \langle +|$  and

 $ho_S^2(0) \equiv |-\rangle \langle -|$ , the eigenstates of the Pauli operator  $\sigma_x$ . The environment is prepared in a motional thermal state  $\rho_E(0)$ , characterized by very low average occupation numbers,  $\bar{n_i} \sim 0.05$  for i=1,2. In practice, this corresponds essentially to the vibrational ground state in both the x and y directions. We then fix the laser parameters to a given pair  $(\Omega, \delta)$  and allow the system to evolve for a time t, at which point we measure the expectation values

$$\langle \sigma_l(t) \rangle, \quad l = x, y, z.$$
 (6)

Each average is obtained from 600 experimental repetitions (cycles), each comprising Doppler and sideband cooling, spin-state initialization, resonant spin-motion interaction, coherent spin rotations, and state-selective fluorescence detection. From these measurements, we reconstruct  $\rho_S^{1,2}(t)$  using Eq. (6) and subsequently compute the trace distance  $D(\rho_1, \rho_2)$  using Eq.(3).

Fig. 2(a) provides an illustrative view of the evolution of  $\rho_S^{1,2}(t)$  and  $D(\rho_1,\rho_2)$ , corresponding to the type of non-Markovian dynamics observed experimentally, as shown in Fig. 2(b). In this panel, we present both the numerically simulated and experimentally measured trace distance dynamics, with each data point obtained as described above. In the experiments, we observed that the dephasing rate  $\gamma$  in Eq. (2) is quite sensitive to trap characteristics, such as the angular frequencies  $\nu_1$  and  $\nu_2$ , as well as to the initial qubit state. This behavior is typical of effective dephasing, which results from several factors, including power-induced heating, photon scattering, and motional decoherence. Careful experimental investigation showed that for our current setup, the dephasing rate for  $\rho_S^1(0) = |+\rangle \langle +|$  is  $\gamma_1 = 0.0049$ , MHz, while for  $\rho_S^2(0) = |-\rangle \langle -|$ , it is  $\gamma_2 = 0.0008$ , MHz. These are the values used in the simulation that fits the experimental data in Fig. 2(b) and (c). Once  $D(\rho_1, \rho_2)$  is determined, we compute its time derivative  $\sigma_t$  (Eq. 4) using central finite differences. The result is displayed in Fig. 2(c), together with the simulation using the parameters discussed above. Finally, we adopted a minimum time step of 0.5,  $\mu$ s to balance accuracy and experimental feasibility. We will return to this point later, when discussing the experimental determination of NM. Finally, the chosen pair  $(\delta, \Omega)$  was  $\delta = 0$  and the Rabi frequency  $\Omega/(2\pi) = 2.245 \, \text{MHz}.$ 

The non-Markovianity (NM) is evaluated by summing the  $\sigma_t$  values that lie above the black dotted line (see Fig. 2(c)), in accordance with Eq. (5). Statistical uncertainties are also included in this analysis [31, 44]. The characterization of NM in our experiments is influenced by several key parameters, as illustrated in Fig. 3. Fig. 3(a) shows the evolution time, defined as the duration for which the Hamiltonian H is applied to the system. As this time increases, NM rises sharply before the rate of growth slows down. Within our experimental capabilities, we choose 100  $\mu s$  as the optimal time window

to run the experiment. The effect of time-step resolution within this window is depicted in Fig. 3(b). NM increases exponentially with finer resolution and tends to saturate beyond 200 points, corresponding to a 0.5  $\mu s$ step. Again aiming to balance accuracy and experimental demands, we adopt a minimum time step of  $0.5 \mu s$ . Fig. 3(c) presents the dependence of NM on the number of experimental repetitions. We observe good stability already around 50 iterations. Accordingly, we use over 500 repetitions to ensure statistical robustness while keeping experimental effort manageable. Finally, Fig. 3(d) shows the influence of the dephasing rates on NM. In this numerical simulation, the dephasing rate of the minus state is fixed at the experimental value  $0.0008 \nu$ , while the dephasing rate of the plus state is varied. The plot includes a special marker indicating the NM value obtained when the plus state's dephasing rate is set to its experimental value. This approach allows us to analyze how NM depends on changes in the plus state's dephasing while accounting for the realistic dephasing of the minus state.

One might intuitively expect that, for a fixed detuning  $\delta$ , the non-Markovianity (NM) would increase monotonically with the coupling strength  $\Omega$ . Contrary to this expectation, our results reveal a non-monotonic dependence of NM on  $\Omega$ . Specifically, NM increases with  $\Omega$  initially, but begins to decrease once  $\Omega$  exceeds the motional frequency  $\nu_i$  of the ion. This behavior highlights a transition in the system's dynamics, emphasizing the nontrivial role of strong coupling in the emergence of memory effects.

Another interesting feature takes place for  $\delta \leq \nu$ , where the maxima of the NM appear to follow a circular pattern. This circular sector is characterized by

$$\delta^2 + \Omega^2 = \nu^2. \tag{7}$$

The most striking feature of this parameter combination is that, when the equality is satisfied, the interaction Hamiltonian Eq. (1) has an effective Jaynes-Cummings description for the Eq. (7) [9]. This approximation extends to a novel regime beyond the traditional carrier and sideband regimes [44].

In the model above, we consider a single ion coupled to a single vibrational mode. However, this framework naturally extends to systems with multiple motional modes, as demonstrated in our experimental investigation with two modes. Here, the non-monotonic dependence of NM with  $\Omega$  persists, and the circular condition  $\delta^2 + \Omega^2 = \nu_i^2$  emerges for each mode.

The previous results have the laser power or equivalently the Rabi frequency fixed as  $\Omega/(2\pi) = 2.245 \,\mathrm{MHz}$ , which is about the same magnitude of the trap frequencies, clearly indicating that we are running experiments in a new regime where the rotating wave approximations leading to the usual carrier and sideband interaction do not apply [9]. To deep our understand o this new regime, we now probe it the non-Markovianity over a range of Rabi frequencies  $\Omega$ . For vibrational mode frequencies

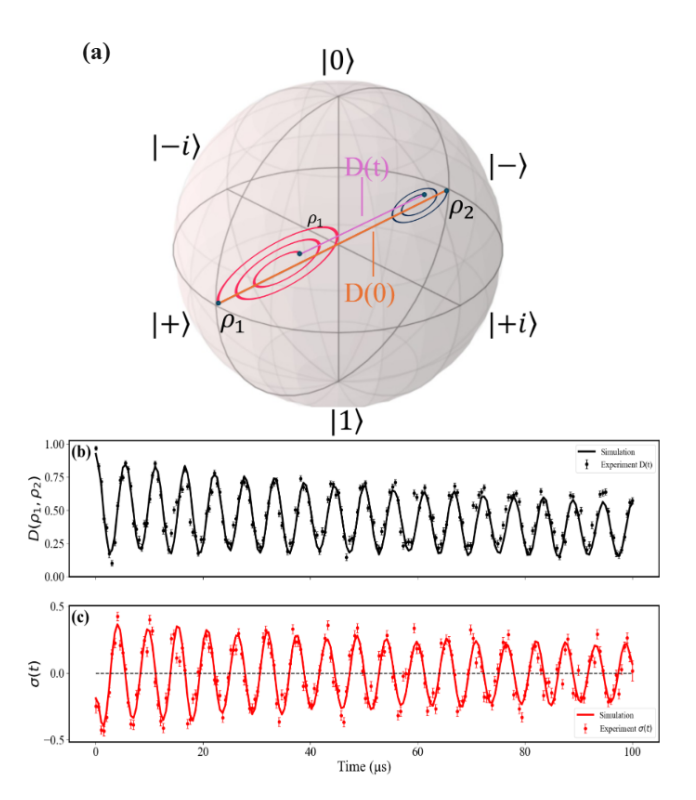


FIG. 2. Dynamics of trace distance and its gradient. (a) Evolution of quantum states  $\rho_1 = |+\rangle \langle +|$  and  $\rho_2 = |-\rangle \langle -|$  on the Bloch sphere, illustrating the gradual loss of distinguishability over time. Here,  $|0\rangle$ ,  $|1\rangle$ ,  $|+\rangle$ ,  $|-\rangle$ ,  $|+i\rangle$ , and  $|-i\rangle$  are eigenstates of the Pauli operators  $\sigma_z$ ,  $\sigma_x$ , and  $\sigma_y$ . (c) Time evolution of the trace distance  $D(\rho_1, \rho_2)$  (Eq. 3), revealing its steady decay. (d) Gradient of the trace distance  $\sigma(t)$  (Eq. 4), as a function of time, highlighting the rate at which the states become indistinguishable. The horizontal black dashed line indicates a threshold: the sum of  $\sigma(t) > 0$  values above this line contributes to non-Markovianity (NM). In all panels, solid curves represent simulation results, and data points correspond to experimental values with corresponding error bars.

 $\nu_1(\nu_2) = 2.32 (3.16) \,\mathrm{MHz}$ , with Lamb-Dicke parameters  $\eta_1(\eta_2) = 0.069 (0.072)$ , and a decay rate  $\gamma = 0.0049$ , spinstate tomography was performed under resonant conditions ( $\delta = 0$ ) to reconstruct the system's density matrix. The trace distance between two initially orthogonal states was evaluated, and its time derivative (Eq. 4) was used to quantify NM via integration over regions where  $\sigma_t > 0$ . Fig. 4 reveals experimental evidence of the theoretically predicted non-monotonic dependence of NM on the coupling strength  $\Omega$ . As  $\Omega$  increases, NM rises, indicating a transition from Markovian to non-Markovian dynamics. This enhancement stems from amplified oscillations of the trace distance due to strong systemenvironment interaction. Notably, when  $\Omega$  exceeds the motional mode frequency  $\nu_i$ , NM decreases, highlighting the intricate interplay between spin and motional degrees of freedom in the strong-coupling regime. For weaker drive fields (lower  $\Omega$ ), a bias of approximately 1 was ob-

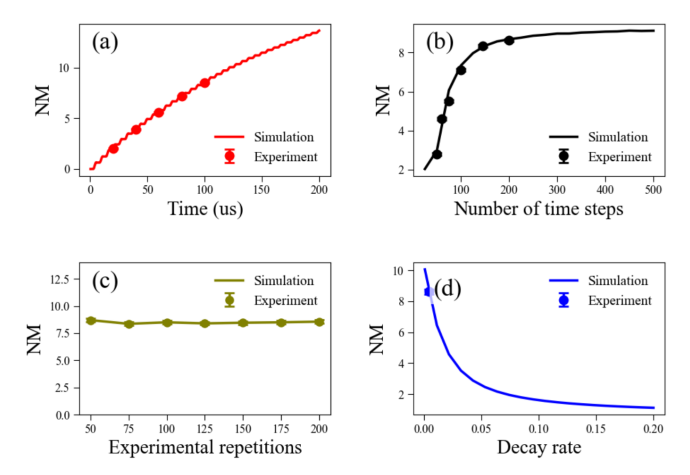


FIG. 3. Non-Markovianity (NM) characterization under varying conditions. (a) Dependence of NM on the total evolution time (with  $0.5\,\mu s$  resolution). (b) Influence of the number of time steps on NM, for a fixed total evolution time of  $100\,\mu s$ . (c) Convergence of NM with respect to the number. (d) Numerical simulation showing NM versus the plus-state dephasing rate, with the minus-state dephasing fixed at the experimental value  $0.0008\,\nu$ . A special marker indicates the NM for the experimental plus-state dephasing.

served. In contrast, at higher drive strengths, two issues become prominent: (i) ionization of the trapped ion, may be attributed to multiphoton ionization (MPI), and (ii) a higher decay rate, seems to be driven by power-induced heating, photon scattering, and motional decoherence. To reduce the chances of ionization, the evolution time was reduced to 40  $\mu s$  for  $\Omega$  near to the motional mode, as shown by the blue curve of Fig. 4. However, even with the reduced evolution time, the decay rate continued to rise with increasing the coupling strengths. This heightened decay could result from a combination of power broadening, dephasing, AC Stark shifts, and heating-induced decoherence.

To demonstrate a unique mapping for each pair of  $(\delta, \Omega)$ , at a specific motional state, where NM exhibits local maxima along a circular pattern (Eq. (7)) consistent with the effective Jaynes-Cummings description, we performed spin-state tomography in the interaction picture for  $40 \,\mu s$  with a time resolution of  $0.25 \,\mu s$ . The results were then transformed into the laboratory frame [44]. Measurements at various detunings require precise calibration, careful parameter control, and extensive experimental repetitions and averaging to ensure statistical reliability. Consequently, four carefully chosen detuning values ( $\delta = 0.25, 1.37, 2.32, \text{ and } 3.16$ ) were selected to balance experimental feasibility with obtaining comprehensive evidence predicted by the circular condition  $\delta^2 + \Omega^2 = \nu_i^2$  (Eq. (7)). Fig. 5 illustrates two circular patterns representing the non-Markovianity in the parameter space of  $(\delta, \Omega)$ , where the smaller pattern corresponds to the mode with frequency  $\nu_1$ , and the larger one to  $\nu_2$ .

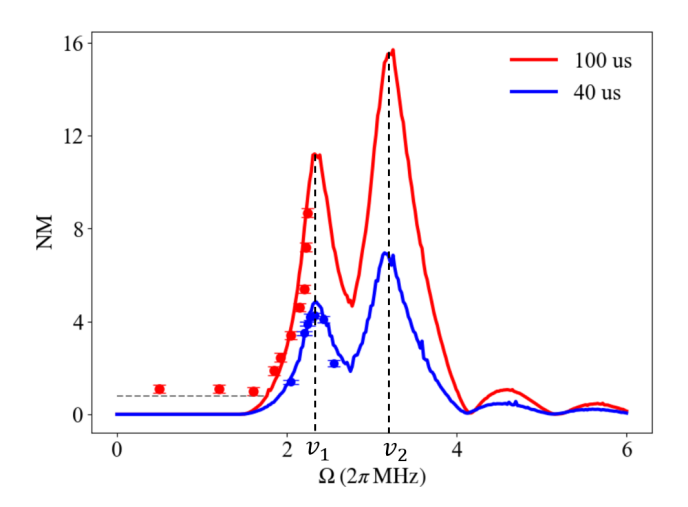


FIG. 4. Non-Markovianity (NM) behavior versus coupling strength  $(\Omega)$  of the resonant laser field  $(\delta = 0)$  at time resolution of  $0.5 \,\mu s$ . The red curve (top) corresponds to an evolution time of 100  $\mu s$ . Non-Markovianity (NM), a sensitive probe to unveil strong-field dynamics, initially increases with the coupling strength  $\Omega$ , indicating a transition from Markovian to non-Markovian behavior due to information backflow from the environment to the system. However, once  $\Omega$  exceeds the vibrational mode frequency  $\nu_i$ , NM begins to decrease, revealing a reversal in this trend. The blue curve (lower) highlights experimental data for  $\Omega$  values near to motional mode with an evolution time of  $40 \,\mu s$ . The reduced evolution time reflects the operational constraints imposed by second ionization and Rabi oscillations power decay, which limit the observation window for non-Markovian dynamics. The curves correspond to simulation results, swith experimental data represented by points.

Points A (yellow), B (red), C (orange), and D (purple) mark distinct  $(\delta, \Omega)$  pairs, with experimental/simulated NM values of 2.0/0.15, 5.0/4.0, 5.7/4.7, and 3.7/0.7, respectively. An inset in Fig. 5 further demonstrates NM as a function of  $\Omega$  for these detuning values, revealing the characteristic behavior of each point. These results demonstrate excellent agreement with the circular condition, providing compelling experimental confirmation of the theoretically predicted structure.

Conclusions. The strong-field regime in quantum systems is fundamentally significant as it reveals non-linear and non-perturbative effects that remain inaccessible in weak-driving conditions. We treat the trapped-ion spin as an open system coupled to two motional modes acting as an interacting environment. Using the spin state tomography under resonant strong-field interactions, we employ non-Markovianity (NM) as a probe to investigate the dynamics of a trapped-ion system. Through systematic variation of  $\Omega$  and detuning  $\delta$ , we observe pronounced deviations from purely Markovian dynamics, emphasizing the role of memory effects arising from the coupling between internal and motional degrees of freedom. Our results demonstrate that NM does not exhibit

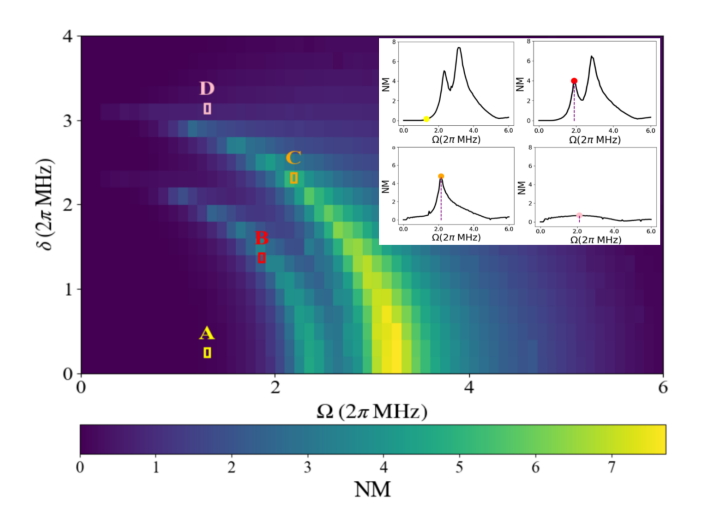


FIG. 5. Experimental results demonstrating the circular pattern of NM maxima as a function of detuning  $(\delta)$  and coupling strength  $(\Omega)$ , satisfy the relation  $\delta^2 + \Omega^2 = \nu^2$ . The insets provide experimental results for specific detuning values:  $\delta = 0.25$ , 1.37, 2.32, and 3.16, corresponding to points A, B, C, and D, respectively. The smaller circular pattern corresponds to the mode with frequency  $\nu_1$ , and the larger one to  $\nu_2$ . These insets show the detailed NM dynamics at each selected point. Experiments were performed with an evolution time of  $40\,\mu\text{s}$ , sampled at 200 steps for high temporal resolution. The detuning effect was implemented in the interaction frame by applying the laser field, while the quantification of NM was carried out by back-transforming the experimental data to the lab frame.

a simple monotonic increase with  $\Omega$  but instead reaches a maximum at the motional mode frequencies. Furthermore, for different parameter pairs  $(\delta, \nu)$ , NM displays a complex dependence on system parameters. Strikingly, when the condition  $\delta^2 + \Omega^2 = \nu^2$  is satisfied, NM exhibits a circular pattern of maxima, corresponding to a transformed Jaynes-Cummings-like interaction. These findings extend beyond the conventional carrier and sideband regimes, revealing new aspects of strong-field quantum dynamics [9, 10]. By using Non-Markovianity as a sensitive probe, we uncover an unexplored dynamical regime, offering deeper insight into quantum behavior under strong driving in trapped-ion platforms.

The authors acknowledge Fernando Semiao, and Tadeu Tassis for valuable theoretical support. This work was supported by the Innovation Program for Quantum Science and Technology under Grants No.2021ZD0301602 and the National Natural Science Foundation of China under Grants No.92065205 and No.62335013.

## Supplementary Information: Realization of Trapped Ion Dynamics in the Strong-Field Regime and Non-Markovianity

#### THEORETICAL DETAILS

Trapped-ions platforms offer exquisite control over multiple degrees of freedom, making them ideal for probing complex quantum dynamics. In particular, we show how non-Markovianity functions as a sensitive probe to diagnose these dynamics under the strong-field regime, where the Rabi frequency  $\Omega$  approaches the motional mode frequency  $\nu$  at resonant conditions. We consider the simplest open quantum system consisting of two-levels interacting with a single harmonic oscillator mode, which acts as the environment. The combined system is assumed to be isolated from external decoherence sources. In a frame rotating at the laser frequency  $\omega_L$ , the system Hamiltonian reads:

$$H_S = \frac{\hbar \delta}{2} \sigma_z, \tag{S1}$$

where  $\delta = \omega_0 - \omega_L$  is the detuning,  $\sigma_z$  is the usual Pauli matrix, and  $\hbar$  is Planck's constant. The environment is modeled as a quantized vibrational mode:

$$H_E = \hbar \nu a^{\dagger} a, \tag{S2}$$

with  $\nu$  the mode frequency and  $a, a^{\dagger}$  the annihilation and creation operators. The interaction Hamiltonian, describing laser-induced spin-motion coupling, is given by:

$$H_I = \frac{\hbar\Omega}{2} \left( \sigma_+ e^{i\eta(a+a^{\dagger})} + \text{h.c.} \right), \tag{S3}$$

where  $\Omega$  is the Rabi frequency,  $\sigma_{\pm}$  are the spin ladder operators,  $\sigma_{x,y}$  signify the Pauli Matrices and  $\eta$  is the Lamb-Dicke parameter. It determines the strength of the coupling between the spin and motion. It is defined as:

$$\eta = k\sqrt{\frac{\hbar}{2m\nu}},\tag{S4}$$

where k is the wavevector of the laser, m is the ion's mass, and  $\nu$  is the trap frequency. The full Hamiltonian, in the rotating frame, becomes:

$$H = \frac{\hbar \delta}{2} \sigma_z + \hbar \nu a^{\dagger} a + \frac{\hbar \Omega}{2} \left( \sigma_+ e^{i\eta(a+a^{\dagger})} + \text{h.c.} \right). \quad (S5)$$

In the presence of Markovian qubit dephasing, the dynamics of a trapped-ion system are governed by the following master equation:

$$\frac{d\rho}{dt} = -i[H, \rho] + \gamma \left(\sigma_z \rho \sigma_z - \rho\right), \tag{S6}$$

where H as given by Eq. S5,  $\rho$  is the density matrix and  $\gamma$  is the dephasing rate. The non-Markovianity (NM) [43] in this context will appear when we trace out the motional degrees of freedom, yielding the reduced qubit state:

$$\rho_{\text{qubit}} := \text{tr}_{\text{mot}}[\rho]. \tag{S7}$$

To detect non-Markovianity (NM), we calculate the trace distance between two qubit states:

$$D(\rho_1, \rho_2) := \frac{1}{2} \text{tr} |\rho_1 - \rho_2|,$$
 (S8)

where  $|A| := \sqrt{A^{\dagger}A}$ . This distance measure has the property that it is monotonically decreasing for any Markovian process  $\Lambda_{t,0}$ :

$$D(\Lambda_{t,0}\rho_1, \Lambda_{t,0}\rho_2) \le D(\rho_1, \rho_2). \tag{S9}$$

Therefore, we can use the time derivative, implementing the central differences, of of the trace distance, denoted as  $\sigma(t)$ , to detect NM:

$$\sigma(t) := \frac{d}{dt} D\left(\Phi_{t,0}\rho_1, \Phi_{t,0}\rho_2\right). \tag{S10}$$

Non-Markovianity can be quantified by integrating over the intervals where  $\sigma(t) > 0$  and optimizing over the initial states  $\rho_1$  and  $\rho_2$ :

$$N(\Phi) := \max_{\rho_1, \rho_2} \int_{\sigma > 0} dt \, \sigma(t). \tag{S11}$$

The maximization is performed over pairs of orthogonal pure states, typically antipodal states on the Bloch sphere. These states can be written as:

$$|\psi_1\rangle = \cos\frac{\theta}{2}|e\rangle + e^{i\phi}\sin\frac{\theta}{2}|g\rangle,$$
 (S12)

$$|\psi_2\rangle = \sin\frac{\theta}{2}|e\rangle - e^{-i\phi}\cos\frac{\theta}{2}|g\rangle.$$
 (S13)

The final step in the process involves maximizing over the angles  $\theta$  and  $\phi$ . In Fig. S1, we show the time evolution of  $\sigma(t)$ , which quantifies non-Markovianity (NM), for initial states  $\rho_1 = |g\rangle \langle g|$  and  $\rho_2 = |e\rangle \langle e|$  over 100  $\mu$ s with a resolution of 0.5  $\mu$ s. The parameters include a Lamb-Dicke parameter  $\eta = 0.069$ , dephasing rate  $\gamma = 0.004$ , detuning  $\delta = 0$ , single-mode frequency  $\nu = 2\pi \times 2.32$  MHz,

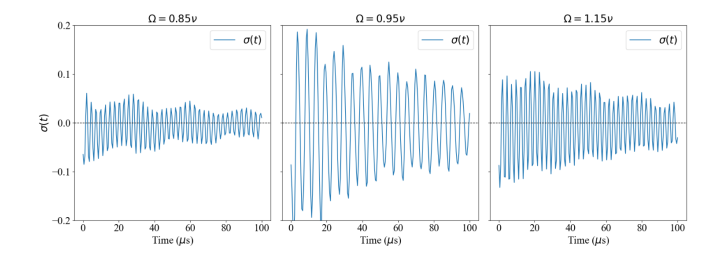


FIG. S1. Numerical calculation of  $\sigma(t)$  for  $\delta=0$ . The positive values, above the dashed line, are a signature of non-Markovianity. For this simulation, the system was initialized in  $\rho_1=|g\rangle\langle g|$  and  $\rho_2=|e\rangle\langle e|$ . The Lamb-Dicke parameter was set to  $\eta=0.069$ , the dephasing rate to  $\gamma=0.004$ , and the motional state was initialized in a thermal state with  $\langle n\rangle=0.05$ .

and a thermal motional state with  $\langle n \rangle = 0.05$ . Coupling strengths were set to  $\Omega = 0.85\nu$ ,  $0.95\nu$ , and  $1.15\nu$ . Positive values of  $\sigma(t)$  indicate non-Markovian dynamics.

To explore the dependence of NM on the Rabi coupling  $\Omega$ , numerical simulations were conducted for various qubit initial states  $(|q\rangle, |e\rangle, |+\rangle, |-\rangle, |+i\rangle, |-i\rangle)$ and motional states. Fig. S2 illustrates the variation of NM with  $\Omega$  under three motional conditions: a thermal state ( $\langle n \rangle = 0.05$ ), a coherent state ( $\alpha = 1$ ), and the vibrational ground state (n = 0). The system exhibits a non-monotonic relationship between NM and  $\Omega$ : at low  $\Omega$ , dynamics are predominantly Markovian, as reflected by small or negligible  $\sigma(t)$  values. Increasing  $\Omega$  leads to a transition into a non-Markovian regime, characterized by significant positive  $\sigma(t)$ . However, for  $\Omega$  exceeding the vibrational frequency, NM decreases due to enhanced dissipation and reduced memory effects. The sensitivity of NM to both motional states and qubit initial conditions is evident. The vibrational ground state (n = 0)shows the strongest NM effects, likely due to its minimal environmental interaction and discrete energy spectrum, which enhance memory retention. The thermal state  $(\langle n \rangle = 0.05)$  displays intermediate NM, balancing environmental interactions and energy distribution. For the coherent state ( $\alpha = 1$ ), NM remains generally low across all qubit states, with a V-shaped dependence on  $\Omega$ . The lowest NM occurs near the mode frequency  $(\nu)$ , where resonant coupling to the environment enhances dissipation and suppresses memory effects. Fig. S3 displays the experimental results for NM vs.  $\Omega$  for 40  $\mu s$ .

An intriguing feature of the dynamics emerges when  $\delta \leq \nu$ , where the degree of non-Markovianity (NM) exhibits a novel circular pattern. This structure is governed by the relation  $\delta^2 + \Omega^2 = \nu^2$ , indicating an underlying symmetry in the parameter space. Notably, when this equality holds, the Hamiltonian in Eq. (S5) can be approximated by the Jaynes-Cummings Hamiltonian in a transformed frame [9]. The motional mode frequencies are given as  $\nu_1(\nu_2) = 2\pi \times 2.32(3.16)\,\mathrm{MHz}$ , with corre-

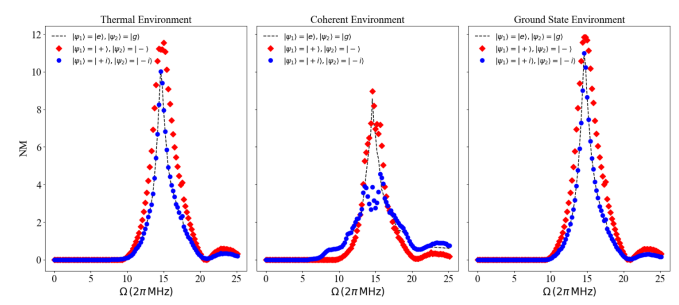


FIG. S2. Non-Markovianity (NM) as a function of the Rabi coupling  $\Omega$  for various initial states of the qubit:  $|g\rangle$ ,  $|e\rangle$ ,  $|e\rangle$ ,  $|+\rangle$ ,  $|-\rangle$ ,  $|+i\rangle$ , and  $|-i\rangle$ . The figure is organized into one row and three columns: (left) the motional state is a thermal state with  $\langle n \rangle = 0.05$ , (middle) the motional state is a coherent state with  $\alpha = 1$ , and (right) the motional state is in the vibrational ground state (n=0). Parameters:  $\nu = 2\pi \times 2.32\,\mathrm{MHz}$ ,  $\gamma = 0.004$ ,  $\eta = 0.069$ , evolution time  $100\,\mu\mathrm{s}$ , and  $200\,\mathrm{time}$  steps.

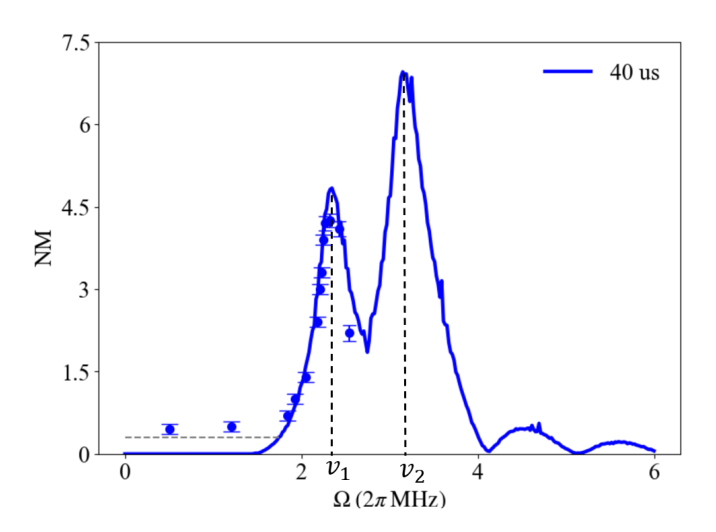


FIG. S3. Non-Markovianity (NM) behavior versus coupling strength  $(\Omega)$  of the resonant laser field  $(\delta=0)$  at a time resolution of 0.5  $\mu s$ . Initially, NM increases with the coupling strength  $\Omega$ . Once  $\Omega$  exceeds the vibrational mode frequency  $\nu_i$ , NM begins to decrease, revealing a reversal in this trend.

sponding Lamb-Dicke parameters  $\eta_1(\eta_2)=0.069(0.072)$  and the time of evolution is  $40~\mu S$  with 2500 time steps. In Fig. S4, each point represents the degree of NM associated with a specific map. Experimentally determining these values involves initializing the motional state, evolving the system under controlled conditions, performing quantum state tomography on the qubit, extracting the time evolution of  $\sigma(t)$ , and integrating its positive contributions. This phenomenon extends beyond conventional carrier and sideband regimes, offering a novel avenue for control in trapped-ion systems. Furthermore, the non-monotonic dependence of NM on  $\Omega$  and the emergence of the circular pattern can be generalized to multiple motional modes, as demonstrated

in our experimental investigation involving two motional modes.

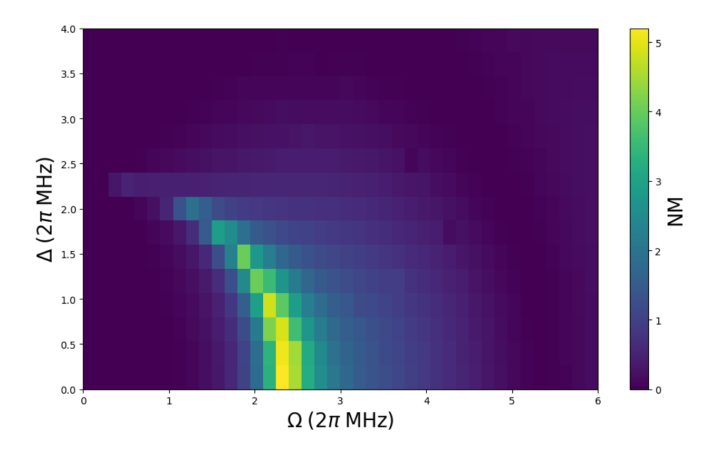


FIG. S4. Numerical calculation of the degree of non-Markovianity  $N(\Phi)$  as a function of the detuning  $\delta$  and coupling strength  $\Omega$ . The time evolution spans  $40\,\mu\mathrm{s}$ , sampled at 250 steps. Parameters used are  $\nu_1(\nu_2)=2.32\times 2\pi\,\mathrm{MHz}$ , Lamb-Dicke parameters  $\eta_1=0.069$ , dephasing rate  $\gamma=0.001\nu$ , and the motional state initialized at the ground state with  $\langle n\rangle=0.05$ .

#### DYNAMICS UNDER STRONG FILED

A single trapped ion interacting with a strong-field resonant laser on the carrier transition experiences dressedstate splitting due to the AC Stark shift. Under the resonance condition  $\Omega \approx \nu$ , the system exhibits coherent population transfer between the ion's internal and motional degrees of freedom [7, 8]. This leads to an effective Javnes-Cummings-like interaction, which provides a novel mechanism for motional state control using a carrier-resonant laser [9]. Fig. S5 illustrates the time evolution of the qubit observables  $\langle \sigma_x \rangle$ ,  $\langle \sigma_y \rangle$ , and  $\langle \sigma_z \rangle$ for for qubit initialized in different states namely:  $|g\rangle$ ,  $|e\rangle, \ |\pm\rangle_{y}, \ {\rm and} \ \ |\pm\rangle_{x} \ {\rm under \ weak\mbox{-}field \ evolution.}$  In contrast, Fig. S6 presents the corresponding dynamics for the strong-field regime, where the Rabi frequency  $\Omega$  is comparable to the motional frequency. As evident, in the strong-field regime, an additional resonance emerges, significantly altering the transition dynamics. This effect underscores the profound impact of strong-field interactions on the system's evolution, extending beyond the conventional weak-driving limit.

#### EXPERIMENTAL SETUP: <sup>171</sup>YB<sup>+</sup> TRAPPED-ION SYSTEM

We confine <sup>171</sup>Yb<sup>+</sup> ions using a *linear Paul trap*, where the qubit states are encoded in the hyperfine levels of the

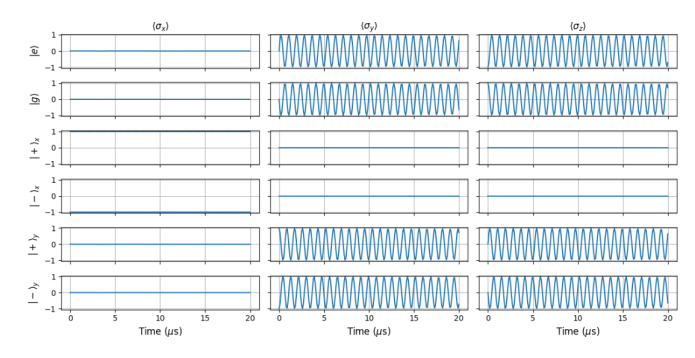


FIG. S5. Time evolution of  $\langle \sigma_x \rangle$ ,  $\langle \sigma_y \rangle$ , and  $\langle \sigma_z \rangle$  for the qubit initialized in  $|g\rangle$ ,  $|e\rangle$ ,  $|\pm\rangle_y$ , and  $|\pm\rangle_x$  under weak-field evolution ( $\Omega$  < motional frequency). The simulation parameters are: Rabi frequency  $\Omega=1\times 2\pi\,\mathrm{MHz}$ , motional frequency  $\nu=2.32\times 2\pi\,\mathrm{MHz}$ , Lamb–Dicke parameter  $\eta=0.069$ , total evolution time  $t=20\,\mathrm{s}$  with 200 timesteps, spontaneous emission rate  $\gamma=0.004$ , and mean thermal occupation number  $\langle n\rangle=0.09$ .

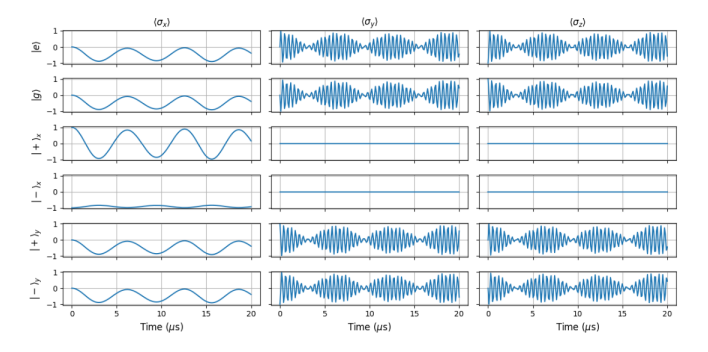


FIG. S6. Time evolution of  $\langle \sigma_x \rangle$ ,  $\langle \sigma_y \rangle$ , and  $\langle \sigma_z \rangle$  for the qubit initialized in  $|g\rangle$ ,  $|e\rangle$ ,  $|\pm\rangle_y$ , and  $|\pm\rangle_x$  under strong-field evolution ( $\Omega \sim$  motional frequency). The simulation parameters are: motional mode frequency  $\nu = 2.32 \times 2\pi$  MHz, Lamb-Dicke parameter  $\eta = 0.069$ , total evolution time t = 20 s with 200 timesteps, spontaneous emission rate  $\gamma = 0.004$ , and mean thermal occupation number  $\langle n \rangle = 0.09$ . An additional resonance emerges due to strong filed regime.

electronic ground state. Specifically, we define:

$$|\downarrow\rangle \equiv |^2 S_{1/2}, F = 0, m_F = 0\rangle,$$
 (S14)

$$|\uparrow\rangle \equiv |^2 S_{1/2}, F = 1, m_F = 0\rangle. \tag{S15}$$

To manipulate and detect qubit states, we employ a 369.5 nm laser for Doppler cooling, optical pumping, and state detection. Coherent qubit control is achieved via two counter-propagating 355 nm Raman laser beams, which also facilitate spin-phonon coupling. Following Doppler cooling, we prepare the phonon modes in their ground state using multi-mode sideband cooling with the same Raman beams. The Raman beams are aligned along the radial direction of the trap, where the anisotropic trapping potential of our Paul trap gives rise

to distinct radial mode frequencies:

$$\nu_1 = 2.32 \,\text{MHz},$$
 (S16)

$$\nu_2 = 3.16 \,\text{MHz}.$$
 (S17)

Further details on the experimental setup and mode frequencies can be found in Ref. [45].

To study the open system's dynamics under interaction with its quantum environment, we initialize the total system in a factorized state,  $\rho_S(0) \otimes \rho_E(0)$ , evolve the system for variable durations t, and perform spin-state tomography. A schematic of the experimental sequence is shown in Fig. S7.

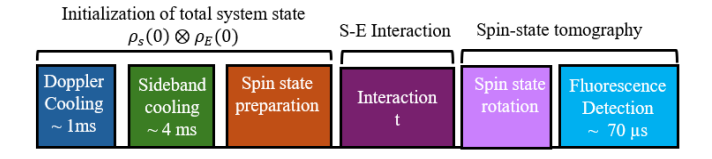


FIG. S7. Experimental sequence (not to scale) implemented to record dynamics of  $\langle \sigma_l(t) \rangle$ , for l=x,y,z. The process begins with preparing factorizing states  $\rho_S(0) \otimes \rho_E(0)$ , followed by S–E interaction enabled by the strong field  $(\Omega \sim \nu_i)$ , with a minimum time resolution of 0.5  $\mu$ s. Spin-state tomography is then performed to characterize the system's evolution.

#### Spin State Initialization

We can precisely initialize the qubit in the eigenstates of  $\sigma_x$ ,  $\sigma_y$ , or  $\sigma_z$  by controlling the *phase* and *duration* of the applied pulses. When the detuning is set to  $\delta = 0$  and the Rabi frequency  $\Omega$  is much smaller than the motional frequency  $\nu$  ( $\Omega \ll \nu$ ), we can make the carrier approximation, which simplifies the Hamiltonian S5 to:

$$H \approx \frac{\Omega}{2} \sigma_x.$$
 (S18)

the evolution operator over a time period  $\tau$  is given by:

$$U_e(\tau) = e^{-iH_e\tau} = \cos\left(\frac{\Omega}{2}\tau\right)I - i\sin\left(\frac{\Omega}{2}\tau\right)\sigma_x.$$
 (S19)

#### Eigenstates of $\sigma_y$

A  $\pi/2$ -pulse is defined by the condition  $\Omega \tau = \pi/2$ . The evolution operator for this case becomes:

$$U_e^{\pi/2} = \cos\left(\frac{\pi}{4}\right)I - i\sin\left(\frac{\pi}{4}\right)\sigma_x = I - \frac{\sqrt{2}}{2}i\sigma_x. \quad (S20)$$

When we apply this  $\pi/2$ -pulse to the qubit states  $|g\rangle$  and  $|e\rangle$ , we obtain:

$$U_e^{\pi/2}|g\rangle = |g\rangle - \frac{\sqrt{2}}{2}i|e\rangle = |-\rangle_y,$$
 (S21)

$$U_e^{\pi/2}|e\rangle = |e\rangle - \frac{\sqrt{2}}{2}i|g\rangle = |+\rangle_y.$$
 (S22)

Thus, after applying the  $\pi/2$ -pulse, the qubit states  $|g\rangle$  and  $|e\rangle$  are mapped to the eigenstates of  $\sigma_y$ , which are  $|+\rangle_y$  and  $|-\rangle_y$ , respectively.

#### Eigenstates of $\sigma_x$

To initialize the eigenstates of  $\sigma_x$ , we perform the same procedure but with a phase shift of  $-\pi/2$ . The evolution operator for a  $\pi/2$ -pulse with this phase shift is:

$$U_e^{\pi/2}(\text{phase} = -\frac{\pi}{2}) = \cos\left(\frac{\pi}{4}\right)I - ie^{-i\pi/2}\sin\left(\frac{\pi}{4}\right)\sigma_x$$
$$= I - \frac{\sqrt{2}}{2}ie^{-i\pi/2}\sigma_x. \tag{S23}$$

This results in the following transformations:

$$U_e^{\pi/2} \left( \text{phase} = -\frac{\pi}{2} \right) |g\rangle = |+\rangle_x,$$
 (S24)

$$U_e^{\pi/2} \left( \text{phase} = -\frac{\pi}{2} \right) |e\rangle = |-\rangle_x.$$
 (S25)

So, after applying a  $\pi/2$ -pulse with the appropriate phase, the qubit states  $|g\rangle$  and  $|e\rangle$  are transformed into the eigenstates of  $\sigma_x$ , which are  $|+\rangle_x$  and  $|-\rangle_x$ , respectively.

# TOMOGRAPHY IN THE INTERACTION FRAME AND TRANSFORMATION TO THE ROTATING FRAME

To implement the trapped ion Hamiltonian in equation S5 with  $\delta \neq 0$ , we use use the interaction form S26 to perform spin tomography

$$H_{\rm int} = \nu a^{\dagger} a + \frac{\Omega}{2} \left( \sigma_{+} e^{i\eta(a+a^{\dagger})} e^{i\delta t + \phi} + \text{h.c.} \right), \quad (S26)$$

once the expectation values of the Pauli matrices  $\langle \sigma_x \rangle$ ,  $\langle \sigma_y \rangle$ , and  $\langle \sigma_z \rangle$  are determined, we apply a back transformation to the lab frame using the time-dependent unitary operator:

$$U(t) = e^{i\frac{\delta}{2}t\sigma_z},\tag{S27}$$

which accounts for the system's evolution due to the detuning  $\delta$ . The expectation values of the Pauli matrices in the lab frame are then given by:

$$\langle \sigma_i \rangle_{\text{lab}} = \text{Tr} \left( U(t) \sigma_i U^{\dagger}(t) \rho \right).$$
 (S28)

The time evolution of the qubit's Pauli expectation values  $\langle \sigma_x \rangle$ ,  $\langle \sigma_y \rangle$ , and  $\langle \sigma_z \rangle$  in the interaction frame, under detuning  $\delta = \nu_2$ , is presented in Fig. S8. Both experimental data and numerical simulations are shown, with labels indicating their origin. Fig. S9 shows the

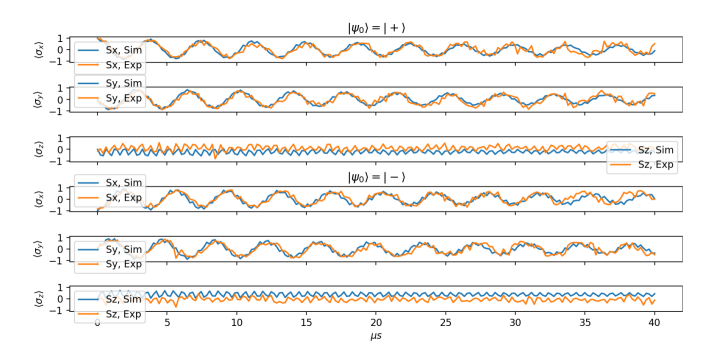


FIG. S8. Evolution of the qubit expectation values  $\langle \sigma_x \rangle$ ,  $\langle \sigma_y \rangle$ , and  $\langle \sigma_z \rangle$  in the interaction frame under detuning  $\delta = \nu_2$ .

same quantities after applying the back transformation using  $U(t)=e^{-i2\delta tS_z}$  for both experimental and simulation data. The detuning  $\delta$  was set to the second motional mode frequency,  $\nu_2=3.16\,\mathrm{MHz}$ , with  $\nu_1(\nu_2)=2.32(3.16)\times 2\pi\,\mathrm{MHz}$ . The Lamb-Dicke parameters were  $\eta_1(\eta_2)=0.069(0.072)$ . The total evolution time was  $40\,\mu\mathrm{s}$ , sampled at intervals of  $0.25\,\mu\mathrm{s}$ .

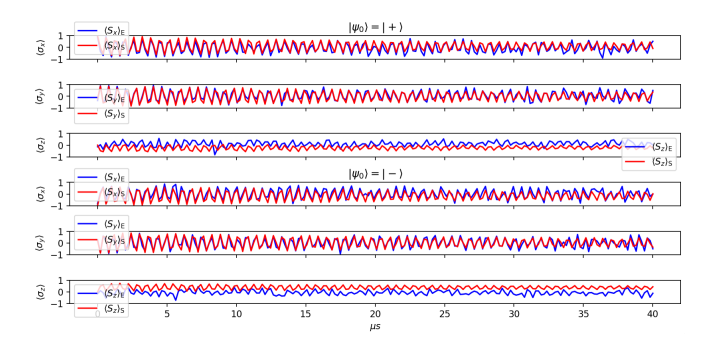


FIG. S9. Expectation values  $\langle \sigma_x \rangle$ ,  $\langle \sigma_y \rangle$ , and  $\langle \sigma_z \rangle$  after applying the back transformation (Eq. (S28)) to return to the lab frame. The results are shown for both experimental data and simulations as indicated by labels.

#### STATISTICAL ERROR ANALYSIS

For each qubit observable  $\langle \sigma_l \rangle \in [-1, 1]$ , the statistical uncertainty due to quantum projection noise (QPN) is estimated assuming binomial statistics:

$$\delta\langle\sigma_l\rangle = 2\sqrt{\frac{p(1-p)}{N}} \tag{S29}$$

where  $p = (\langle \sigma_l \rangle + 1)/2$  and N is the number of measurements [31]. The trace distance between two single-qubit

states is  $D=\frac{1}{2}\|\vec{S}^{(1)}-\vec{S}^{(2)}\|$ , with uncertainty  $\delta D$  obtained via standard error propagation. The time derivative  $\sigma(t)=dD/dt$  is computed numerically using a symmetric finite difference, and its error is

$$\delta\sigma(t) = \frac{1}{\Delta t} \sqrt{\delta D(t + \Delta t)^2 + \delta D(t - \Delta t)^2}$$
 (S30)

Finally, the non-Markovianity measure  $\mathcal{N} = \sum_{\sigma(t)>0} \sigma(t) \Delta t$  has an associated uncertainty

$$\delta \mathcal{N} = \sqrt{\sum_{\sigma(t)>0} (\delta \sigma(t) \, \Delta t)^2}.$$
 (S31)

- \* Corresponding author:krehan2010@yahoo.com
- † Corresponding author: kimkihwan@mail.tsinghua.edu.cn
- D. Leibfried, R. Blatt, C. Monroe, and D. Wineland, Rev. Mod. Phys. 75, 281 (2003).
- [2] H. Häffner, C. F. Roos, and R. Blatt, Phys. Rep. 469, 155 (2008).
- [3] J. I. Cirac and P. Zoller, Phys. Rev. Lett. 74, 4091 (1995).
- [4] C. Monroe, D. M. Meekhof, B. E. King, W. M. Itano, and D. J. Wineland, Phys. Rev. Lett. 75, 4714 (1995).
- [5] M. Gessner, M. Ramm, T. Pruttivarasin, A. Buchleitner, H.-P. Breuer, and H. Häffner, Nature Physics 10, 105 (2014).
- [6] H. Moya-Cessa, A. Vidiella-Barranco, J. A. Roversi, D. S. Freitas, and S. M. Dutra, Phys. Rev. A 59, 2518 (1999).
- [7] D. Jonathan, M. B. Plenio, and P. L. Knight, Phys. Rev. A 62, 042307 (2000).
- [8] D. Jonathan and M. B. Plenio, Phys. Rev. Lett. 87, 127901 (2001).
- [9] T. Tassis and F. L. Semião, Phys. Rev. A 107, 042605 (2023).
- [10] T. Tassis, F. Brito, and F. Semião, APL Quantum 2 (2025).
- [11] A. Rivas, S. F. Huelga, and M. B. Plenio, Phys. Rev. Lett. 105, 050403 (2010).
- [12] H.-P. Breuer, E.-M. Laine, and J. Piilo, Phys. Rev. Lett. 103, 210401 (2009).
- [13] A. K. Rajagopal, A. R. Usha Devi, and R. W. Rendell, Phys. Rev. A 82, 042107 (2010).
- [14] B. Bylicka, D. Chruściński, and S. Maniscalco, Scientific reports 4, 5720 (2014).
- [15] C. Pineda, T. Gorin, D. Davalos, D. A. Wisniacki, and I. García-Mata, Phys. Rev. A 93, 022117 (2016).
- [16] F. F. Fanchini, G. Karpat, B. Çakmak, L. K. Castelano, G. H. Aguilar, O. J. Farías, S. P. Walborn, P. H. S. Ribeiro, and M. C. de Oliveira, Phys. Rev. Lett. 112, 210402 (2014).
- [17] S. Alipour, A. Mani, and A. T. Rezakhani, Phys. Rev. A 85, 052108 (2012).
- [18] H. S. Dhar, M. N. Bera, and G. Adesso, Phys. Rev. A 91, 032115 (2015).
- [19] M. M. Wolf and J. I. Cirac, Communications in Mathematical Physics 279, 147 (2008).
- [20] S. Utagi, R. Srikanth, and S. Banerjee, Scientific Reports 10, 15049 (2020).
- [21] J. Preskill, Quantum 2, 79 (2018).

- [22] B.-H. Liu, L. Li, Y.-F. Huang, C.-F. Li, G.-C. Guo, E.-M. Laine, H.-P. Breuer, and J. Piilo, Nature Physics 7, 931 (2011).
- [23] A. Chiuri, C. Greganti, L. Mazzola, M. Paternostro, and P. Mataloni, Scientific reports 2, 968– (2012).
- [24] K. A. Fisher, R. Prevedel, R. Kaltenbaek, and K. J. Resch, New Journal of Physics 14, 033016 (2012).
- [25] J.-S. Tang, C.-F. Li, Y.-L. Li, X.-B. Zou, G.-C. Guo, H.-P. Breuer, E.-M. Laine, and J. Piilo, Europhysics Letters 97, 10002 (2012).
- [26] H. Lyyra, O. Siltanen, J. Piilo, S. Banerjee, and T. Kuusela, Phys. Rev. A 106, 032603 (2022).
- [27] N. K. Bernardes, A. Cuevas, A. Orieux, C. H. Monken, P. Mataloni, F. Sciarrino, and M. F. Santos, in *Quantum Optics and Quantum Information Transfer and Processing* 2015, Vol. 9505 (SPIE, 2015) pp. 125–131.
- [28] G. A. White, C. D. Hill, F. A. Pollock, L. C. Hollenberg, and K. Modi, Nature Communications 11, 6301 (2020).
- [29] J. M. Gambetta, A. D. Córcoles, S. T. Merkel, B. R. Johnson, J. A. Smolin, J. M. Chow, C. A. Ryan, C. Rigetti, S. Poletto, T. A. Ohki, M. B. Ketchen, and M. Steffen, Phys. Rev. Lett. 109, 240504 (2012).
- [30] G. A. L. White, K. Modi, and C. D. Hill, Phys. Rev. Lett. 130, 160401 (2023).
- [31] M. Wittemer, G. Clos, H.-P. Breuer, U. Warring, and T. Schaetz, Phys. Rev. A 97, 020102 (2018).
- [32] B.-W. Li, Q.-X. Mei, Y.-K. Wu, M.-L. Cai, Y. Wang, L. Yao, Z.-C. Zhou, and L.-M. Duan, Phys. Rev. Lett. 129, 140501 (2022).
- [33] W. Campbell, J. Mizrahi, Q. Quraishi, C. Senko, D. Hayes, D. Hucul, D. Matsukevich, P. Maunz, and C. Monroe, Phys. Rev. Lett. 105, 090502 (2010).

- [34] J. Mizrahi, C. Senko, B. Neyenhuis, K. Johnson, W. Campbell, C. Conover, and C. Monroe, Phys. Rev. Lett. 110, 203001 (2013).
- [35] A. Smith, Y. Lu, S. An, X. Zhang, J.-N. Zhang, Z. Gong, H. Quan, C. Jarzynski, and K. Kim, New J. Phys. 20, 013008 (2018).
- [36] S. An, J.-N. Zhang, M. Um, D. Lv, Y. Lu, J. Zhang, Z.-Q. Yin, H. T. Quan, and K. Kim, Nat. Phys. 11, 193 (2015).
- [37] M. Um, J. Zhang, D. Lv, Y. Lu, S. An, J.-N. Zhang, H. Nha, M. S. Kim, and K. Kim, Nat. Commun. 7, 11410 (2016).
- [38] J. Zhang, M. Um, D. Lv, J.-N. Zhang, L.-M. Duan, and K. Kim, Phys. Rev. Lett. 121, 160502 (2018).
- [39] Y. Shen, Y. Lu, K. Zhang, J. Zhang, S. Zhang, J. Huh, and K. Kim, Chem. Sci. 9, 836 (2018).
- [40] D. Lv, S. An, Z. Liu, J.-N. Zhang, J. S. Pedernales, L. Lamata, E. Solano, and K. Kim, Phys. Rev. X 8, 021027 (2018).
- [41] W. Chen, J. Gan, J.-N. Zhang, D. Matuskevich, and K. Kim, Chinese Physics B 30, 060311 (2021).
- [42] J. Zhang, P. Wang, W. Chen, Z. Cai, M. Qiao, R. Li, Y. Huang, H. Tian, H. Tu, K. Cui, et al., arXiv preprint arXiv:2408.14373 (2024).
- [43] H.-P. Breuer, E.-M. Laine, J. Piilo, and B. Vacchini, Rev. Mod. Phys. 88, 021002 (2016).
- [44] Supplementary materials.
- [45] C.-Y. Luan, Quantum Information Processing with Dualspecies Trapped Ions, Ph.D. thesis, Tshinghua University, Beijing PR China (2024).